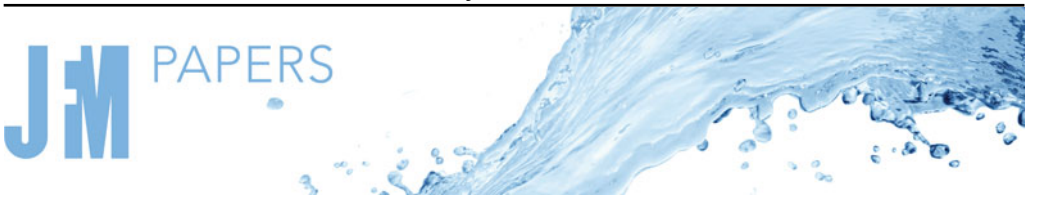
J. Fluid Mech. (2026), *vol.* 1035, A19, doi:10.1017/jfm.2026.11575



Jet formation in air bubbles induced by cavitation bubbles

Shiyu Liu[1,2,†], **Bingqi Wang**[1,2,†], **Shi-Min Li**[1,2], **A-Man Zhang**[1,2], **Cui Pu**[1,2] and **Qingyun Zeng**[1,2]

[1]College of Shipbuilding Engineering, Harbin Engineering University, Harbin 150001, PR China

[2]Sanya Nanhai Innovation and Development Base of Harbin Engineering University, Sanya 572024, PR China

Corresponding authors: Qingyun Zeng, qyzeng@hrbeu.edu.cn; A-Man Zhang, zhangaman@hrbeu.edu.cn; Cui Pu, cuipu@hrbeu.edu.cn

(Received 16 October 2025; revised 19 April 2026; accepted 19 April 2026)

Bubble pairs are effective modulators of liquid jets. We investigate the jetting of an air bubble driven by a laser-induced cavitation bubble using high-speed imaging, compressible volume-of-fluid (VoF) simulations and theoretical analysis. Three distinct jet types emerge, depending on the stand-off distance γ and size ratio η between the bubbles. Jet formation proceeds through two stages: an initial shock-induced acceleration followed by flow focusing on the concave liquid–air interface. We derive scaling relations, $V_0 = 1.1 p_0 R_0/(\rho c R_l)((\gamma(1+\eta)-1)/\eta)^{-1.6}$ for the shock-driven stage and $V_m = (1+(0.8-0.5\gamma)\eta^{0.75})V_0$ for the flow focusing stage in the strong jet regime, both of which agree closely with experimental and numerical measurements. Here, V_0 and V_m denote the velocity increments associated with shock-wave-induced acceleration and flow focusing stages, respectively. The variables p_0, R_0, ρ, c and R_l represent the initial pressure and radius of the cavitation bubble, the fluid density, the speed of sound in the liquid and the maximum volume-equivalent radius of the cavitation bubble, respectively. A (η, γ) phase diagram delineates the weak, strong and explosive jets, with regime boundaries accurately captured by the theoretically derived transitions.

Key words: bubble dynamics, cavitation

1. Introduction

Transient liquid jets emerging from interfaces play a critical role in many natural phenomena and engineering applications (Eggers 1997; Eggers & Villermaux 2008; Lohse 2022), serving as an efficient mechanism for delivering liquid into surrounding media

[†]Both authors contributed equally to the manuscript.

© The Author(s), 2026. Published by Cambridge University Press.

https://doi.org/10.1017/jfm.2026.11575 Published online by Cambridge University Press

either as highly focused jets (Peters *et al.* 2013) or as mono-disperse droplets formed through intrinsic jet instabilities (Visser *et al.* 2012). Jet initiation can arise from various mechanisms, including bubble bursting at a free surface (Lai, Eggers & Deike 2018), impact of solids or droplets on a liquid interface (Gekle *et al.* 2010), focusing of nonlinear Faraday waves (Zeff *et al.* 2000), pressure wave focusing induced by impact (Kiyama *et al.* 2016) and laser-induced cavitation (Tagawa *et al.* 2012), among others. In these scenarios, local high pressure resulting from complex interfacial deformations produces intense accelerations that drive the free surface into rapid jetting. Furthermore, the interplay among surface interactions (Han *et al.* 2015; Fan *et al.* 2024), geometric constraints (Zeng *et al.* 2024) and flow conditions (Mnich *et al.* 2024) provides potential avenues for tailoring jet morphology and velocity.

Jets accelerated by flow focusing effects are highly sensitive to the curvature of the liquid interface (Tagawa *et al.* 2012; Zeng *et al.* 2024). Compared with externally imposed flow geometries, an accessible mechanism for generating strong focusing is the interaction of paired bubbles at different phases (Han *et al.* 2015; Tomita & Sato 2017). For a pair of cavitation bubbles, varying the time interval and distance leads to distinct deformations of the bubble, which in turn modulate the focusing strength and the resulting hydrodynamic pressure. A particularly notable case arises when the bubbles oscillate in anti-phase, with the second bubble nucleated at the instant the first bubble reaches its maximum radius. While early studies reported that the jet velocity in this configuration can reach on the order of $100\,\mathrm{m\,s^{-1}}$ (Han *et al.* 2015; Mishra *et al.* 2022), more recent investigations, with ultra-fast imaging up to five million frames per second (fps), have revealed that at specific distances, the second bubble develops fast needle-like jet with velocities of the order of $1000\,\mathrm{m\,s^{-1}}$ (Fan *et al.* 2024). There during the jet formation, the bubble develops an elongated upper interface prone to tip splitting. This splitting process emits multiple shock waves associated with the rupture and toroidal collapse of the detached cap and the first bubble, which subsequently converge towards the bubble neck. The resulting high pressure region drives the narrow neck interface into a fast needle-like jet. Yet the condition for the formation of a needle-jet is highly restrictive, i.e. the two bubbles must oscillate in exact anti-phase and the dimensionless stand-off distance is limited in a narrow range $0.7 < \gamma < 0.8$.

In contrast, little attention has been given to the interaction between air bubbles and cavitation bubbles. Earlier studies primarily examined the attenuation of shock waves by air bubbles (Luo, Xu & Khoo 2021). Despite the apparent similarity in configuration, the air bubble acts as a stable, curved interface with nearly constant volume, giving rise to a jetting dynamics that is distinct yet not fully understood. In contrast to a pair of cavitation bubbles, whose dynamics is highly sensitive to the relative phase between bubbles, and small timing variations can lead to order-of-magnitude changes in jet velocity and size (Han *et al.* 2015; Fan *et al.* 2024), the interaction between a cavitation bubble and a neighbouring air bubble provides a robust configuration for studying and modulating jet formation. Moreover, interactions between cavitation bubbles and gas bubbles commonly arise in bubbly flows and other fast multiphase flows involving phase change (Maeda & Fuster 2024; Zhang *et al.* 2024). The deformation and jetting of an expanding and collapsing cavitation bubble can significantly influence the motion, oscillation and jetting behaviour of nearby gas bubbles. A fundamental understanding of gas–cavitation bubble interactions at the single-bubble level therefore provides new insight into these phenomena.

In this study, we combine high-speed photography, compressible VoF simulations and theoretical analysis to quantitatively investigate the jetting dynamics in the air bubble arising from the interaction between a laser-induced cavitation bubble and an air bubble.

https://doi.org/10.1017/jfm.2026.11575 Published online by Cambridge University Press

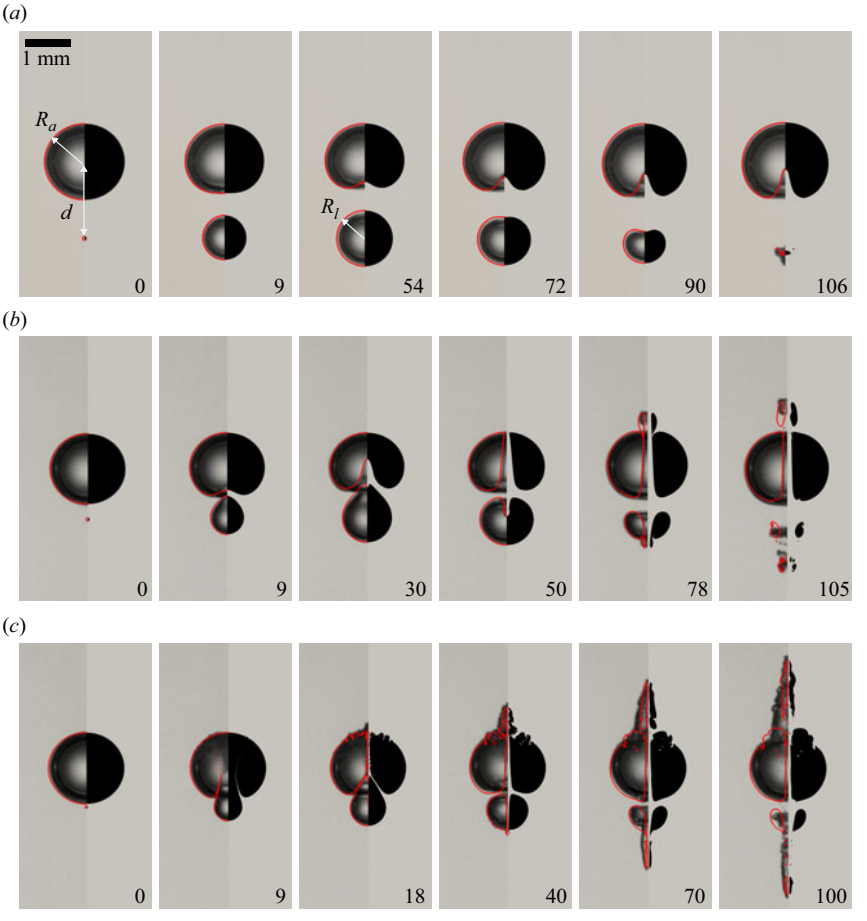


Figure 1. Comparison between experiments (left part of each panel) and simulation (right) for the three represented scenarios. (*a*) Weak jet: experiment, $R_a = 896 \pm 33\,\mu$m, $R_l = 615 \pm 33\,\mu$m, $d = 1755 \pm 33\,\mu$m; simulation, $R_0 = 45\,\mu$m, $R_a = 900\,\mu$m, $R_l = 635\,\mu$m, $d = 1750\,\mu$m; (*b*) strong jet: experiment, $R_a = 909 \pm 33\,\mu$m, $R_l = 599 \pm 33\,\mu$m, $d = 1254 \pm 33\,\mu$m; simulation, $R_0 = 48\,\mu$m, $R_a = 910\,\mu$m, $R_l = 623\,\mu$m, $d = 1250\,\mu$m; (*c*) explosive jet: experiment, $R_a = 953 \pm 33\,\mu$m, $R_l = 564 \pm 55\,\mu$m, $d = 998 \pm 33\,\mu$m; simulation, $R_0 = 40\,\mu$m, $R_a = 950\,\mu$m, $R_l = 546\,\mu$m, $d = 1000\,\mu$m. Numbers denote identical time instances (μs) in experiment and simulation. The computed bubble interface (red contours) is also superimposed in the experimental images.

The results reveal three distinct jetting regimes, which can be organised on a parametric map defined by the stand-off distance γ between the two bubbles and the size ratio η of the cavitation bubble to the air bubble. Specifically, $\gamma = d/(R_a + R_l)$ and $\eta = R_l/R_a$, where d is the centre-to-centre distance, R_a is the air-bubble radius and R_l is the volume-equivalent maximum radius of the laser-induced cavitation bubble, as shown in figure 1.

2. Experiments and simulation

Experiments were conducted in an acrylic water container of 60 mm × 60 mm × 100 mm at an ambient pressure of 1 atm. A stainless steel needle (diameter 0.15 mm) was mounted at the centre of the container's lower wall and connected to a syringe pump (LSP02-3BH) to inject air at a constant flow rate, thereby producing millimetre-sized, nearly spherical air bubbles at the needle tip. Cavitation bubbles were generated in the vicinity of the

https://doi.org/10.1017/jfm.2026.11575 Published online by Cambridge University Press

air bubble by focusing laser pulses from a Q-switched Nd:YAG laser (DPS; wavelength 532 nm, pulse width 6.6 ns). The laser beam was first expanded and collimated using a pair of plano-concave and plano-convex lenses, and subsequently focused with a microscope objective (M Plan Apo L 10×, NA = 0.28). The bubble dynamics was recorded using a high-speed camera (Phantom V2012) operating at 340 000 fps with an exposure time of 1 µs. Uniform background illumination was provided by an LED light source, diffused through a matte glass plate. The camera, equipped with a macro lens (LAOWA 100 mm, f/2.8), achieved a spatial resolution of 33 µm per pixel. In the experiments, the bubble centreline was aligned with the centreline of the camera sensor such that the optical axis was locally normal to the air–liquid interface in the measurement region. Under this condition, refraction-induced geometric distortion is minimal, and its influence on the measured jet-tip velocity is negligible comparing to the uncertainty due to spatial and temporal resolutions. Based on the spatial and temporal resolutions $\Delta L = 33$ µm and $\Delta T = 2.94$ µs, the relative experimental uncertainty in the jet velocity is estimated as $\Delta V_{jet}/V_{jet} = ((\Delta L/L)^2 + (\Delta T/T)^2)$, with L and T denoting the displacement and time interval between two selected measurement instants.

The laser-induced cavitation bubble can be modelled as a gas-filled bubble with an initially high internal pressure, as widely adopted in previous well-validated simulations of its first oscillation cycle (Zeng, An & Ohl 2022). The gas content of both the air and cavitation bubbles is treated in the same manner, while their differing initial pressures and densities give rise to distinct dynamics. The bubble interface is captured through solving a transport equation for α, the volume fraction of the liquid phase:

$$\frac{\partial \alpha}{\partial t} + \nabla \cdot (\alpha \boldsymbol{U}) + \nabla \cdot (\alpha(1-\alpha)\boldsymbol{U_r}) = \alpha(1-\alpha)\left(\frac{\psi_g}{\rho_g} - \frac{\psi_l}{\rho_l}\right)\frac{\mathrm{D}p}{\mathrm{D}t} + \alpha \nabla \cdot \boldsymbol{U}, \qquad (2.1)$$

where variables t, $\boldsymbol{U}$, ρ and p are the time, flow velocity, fluid density and flow pressure, respectively. An artificial compressible term $\boldsymbol{U_r}$ is introduced to adjust the sharpness of the interface. Here, $\psi = \mathrm{D}\rho/\mathrm{D}p$ calculates the flow compressibility based on the equations of state (EoS) for both gas and liquid, with subscripts l and g representing the liquid and gas phases, respectively.

In the simulations, the laser-induced bubble is initialised as a spherical gas pocket of small radius and high internal pressure, while the air bubble is modelled as a stationary sphere with an internal pressure of $p_\infty + 2\sigma/R_a$, with σ the coefficient of surface tension. The gas phase is described by a polytropic equation of state and the liquid phase is treated as a compressible Tait fluid. The transport equation and the compressible Navier–Stokes (NS) equations are solved together in OpenFOAM (Weller *et al.* 1998; Miller *et al.* 2013; Koch *et al.* 2016). Since the problem in this study is axisymmetric, the computational domain is simplified as a wedge with a small angle of 2°. The domain is locally and recursively refined to a grid space of $\Delta x = 2.23$ µm in the area where both bubbles are located. The ambient pressure $p_\infty = 101\,325$ Pa is applied at the top boundary. Vanishing gradient of pressure and velocities are applied at the remaining boundaries to allow in and out flux. During the computing, the time step is adaptively renewed for every PIMPLE algorithm loop according to the specified Courant number $Co = 0.1$ to ensure a stable solution. See Zeng *et al.* (2018, 2022) for more details.

3. Bubble dynamics and jet formation

Figure 1 compares experimental and numerical results for three representative scenarios. In each panel, the left half shows experimental shadowgraphs with superimposed simulation contours (red), while the right half displays the corresponding computed bubble

https://doi.org/10.1017/jfm.2026.11575 Published online by Cambridge University Press

dynamics. At $t = 0$, the cavitation bubble is nucleated at a distance d beneath an air bubble of radius R_a. In the simulations, since the cavitation bubble interior is determined by its initial radius R_0 and pressure p_0, to keep the simulation robust while correctly modelling the pressure induced by an ns laser pulse, $p_0 = 2500$ bar is chosen. So, R_0 is the only parameter adjusted to match experiments. Overall, the comparison in figure 1 has demonstrated close agreement between experiments and simulations in both bubble dynamics and jet morphology across all three jetting regimes. Next, we discuss each type of jet and analyse the underlying jet-formation processes.

For a relatively large distance $\gamma \approx 1.16$ (figure 1*a*), as the cavitation expands and collapses, the proximate surface of the air bubble, which is concave initially, becomes nearly flat and then develops into an upward jet along the symmetry axis. This jet is decelerated by surface tension and viscous drag until its velocity vanishes, before retracting under capillary forces; we refer to this as a weak jet. Meanwhile, the cavitation bubble translates away from the air bubble and generates a downward microjet. Similar jet formation dynamics is observed in a recent work of Bokman *et al.* (2025) on shock-induced bubble dynamics, where reducing the pressure impulse, the integration of pressure over the pulse width, the bubble moves from a jetting regime to a no-jetting regime.

Figures 2(*a*) and 2(*b*) show the vertical movement and velocity of the lower air–bubble interface for $\gamma = 1.14$ and $\eta = 0.70$, denoted y and V_{jet}, respectively. The experimental data for y and V_{jet} are shown as open squares and agree well with the numerical results. The inset of figure 2(*a*) presents the temporal evolution of the lower air–bubble interface at intervals of 10 µs. Overall, the initially lowest point of the air–bubble interface moves upward faster than the surrounding regions, causing the interface to flatten initially and subsequently deform into a convex shape. As shown in figure 2(*a*), y increases gradually, whereas the jet velocity in figure 2(*b*) exhibits a fluctuating behaviour, with a peak value of approximately 11 m s^{-1} attained at an early time, $t \approx 1.04$ µs.

To elucidate the development of the jet tip, the pressure and velocity fields at six representative time instants are shown in panels (*c*)–(*h*). These time instants are also marked by red dots on the curves of y and V_{jet}. The interface velocity begins to rise at $t \approx 0.64$ µs, coinciding with the arrival of the nucleation shock wave (figure 2*c*). The shock front is identified as the location of the maximum pressure gradient along the propagation direction. This wave partially transmits into the air bubble and propagates upward, while a portion of the wave is reflected at the air–liquid interface and travels back into the surrounding liquid. The interface reaches a peak velocity of $\sim$11 m s^{-1} at $t \approx 1.04$ µs, after which the shock-induced pressure gradient dissipates. This peak velocity due to shock-wave-induced acceleration is defined as V_0. Subsequently, V_{jet} fluctuates for approximately 3 µs as pressure waves reflect repeatedly between the two interfaces, alternately accelerating and decelerating the surface. By $t = 4.52$ µs, the jet increases again due to flow focusing and reaches a velocity of $\sim$10 m s^{-1} at $t \approx 12$ µs, before gradually decelerating as surface tension dominates once the interface becomes convex at $t = 50$ µs, restoring the spherical equilibrium shape. We refer to this velocity associated with the flow focusing stage as V_m.

At a smaller separation, $\gamma \approx 0.83$ (figure 1*b*), the air-bubble jet acquires sufficient momentum to overcome surface tension and viscous drag, eventually piercing the upper interface and shedding a toroidal air bubble; this is termed a strong jet.

Figures 3(*a*) and 3(*b*) compare the vertical movement and velocity of the lower air–bubble interface for $\gamma = 0.82$ and $\eta = 0.68$, denoted y and V_{jet}, respectively. The numerical results are shown as blue lines, while the experimental data are plotted as open squares, which are in excellent agreement. The inset of figure 3(*a*) shows the evolution of the lower air–bubble interface at intervals of 2 µs, revealing a more rapid jet development

https://doi.org/10.1017/jfm.2026.11575 Published online by Cambridge University Press

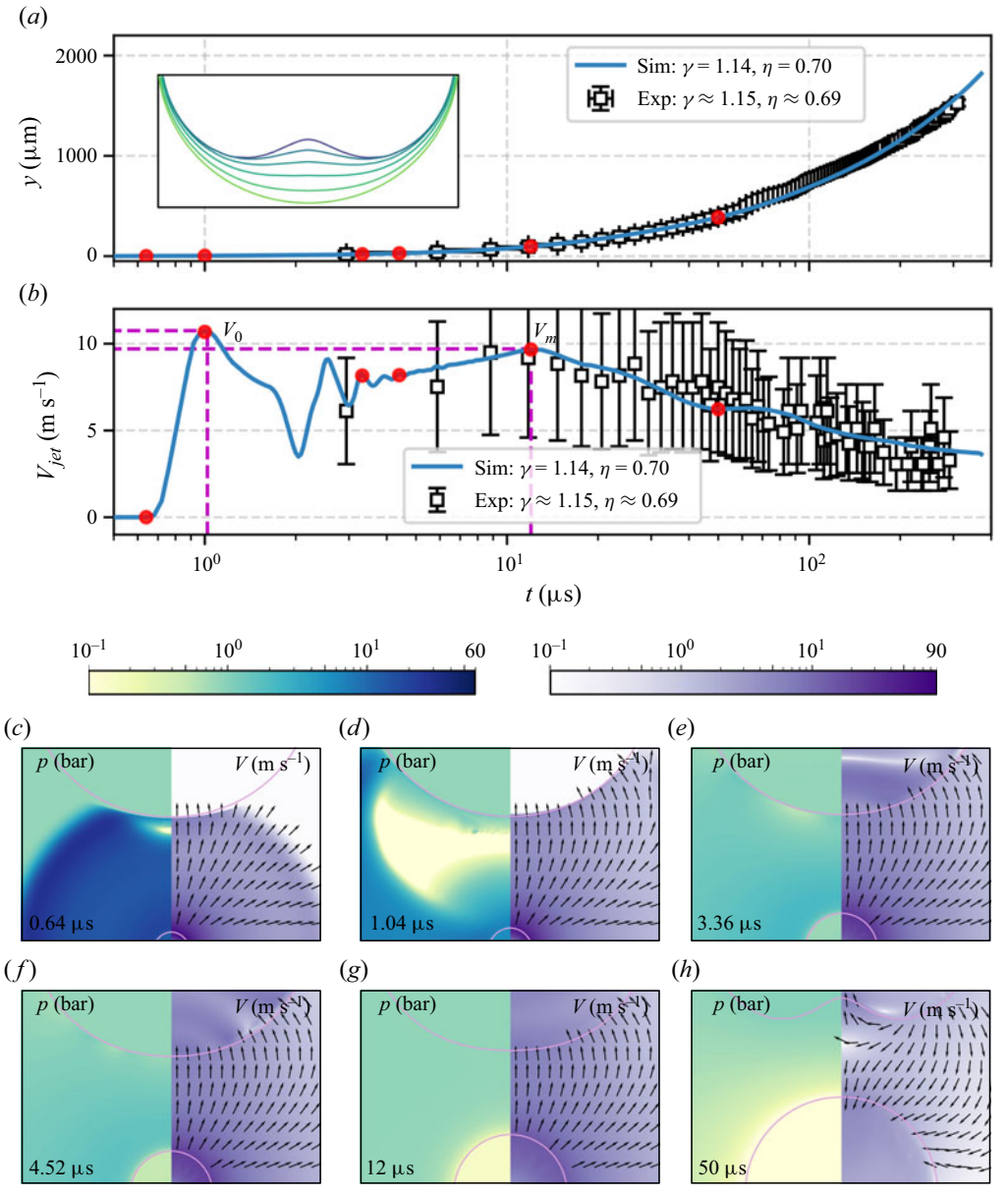


Figure 2. Evolution of a weak jet for a weak jet of $\gamma = 1.14$ and $\eta = 0.70$. (*a*) Vertical displacement of the air-bubble bottom surface and (*b*) jet velocity. The inset in panel (*a*) shows the jet tip deformation with time intervals of 10 μs. The pressure (left) and flow fields (right) are shown for the (*c–e*) initial acceleration stage and (*f–h*) jet focusing stage. Magnitudes are colour-coded and arrows indicate flow directions of the liquid phase. For a clear presentation, arrows in the region of approximately zero velocity are removed. Purple lines denote bubble interfaces in panels (*c−h*). Each frame is 2 mm wide. Time instants for panels (*c−h*) are indicated by red dots in panels (*a*) and (*b*).

than that of the weak jet case shown in figure 2. This faster development is also reflected in figure 3 (*a*), where y increases more rapidly. The corresponding V_{jet} curve exhibits a markedly different behaviour; it first rises rapidly to approximately 32 m s^{-1},

https://doi.org/10.1017/jfm.2026.11575 Published online by Cambridge University Press

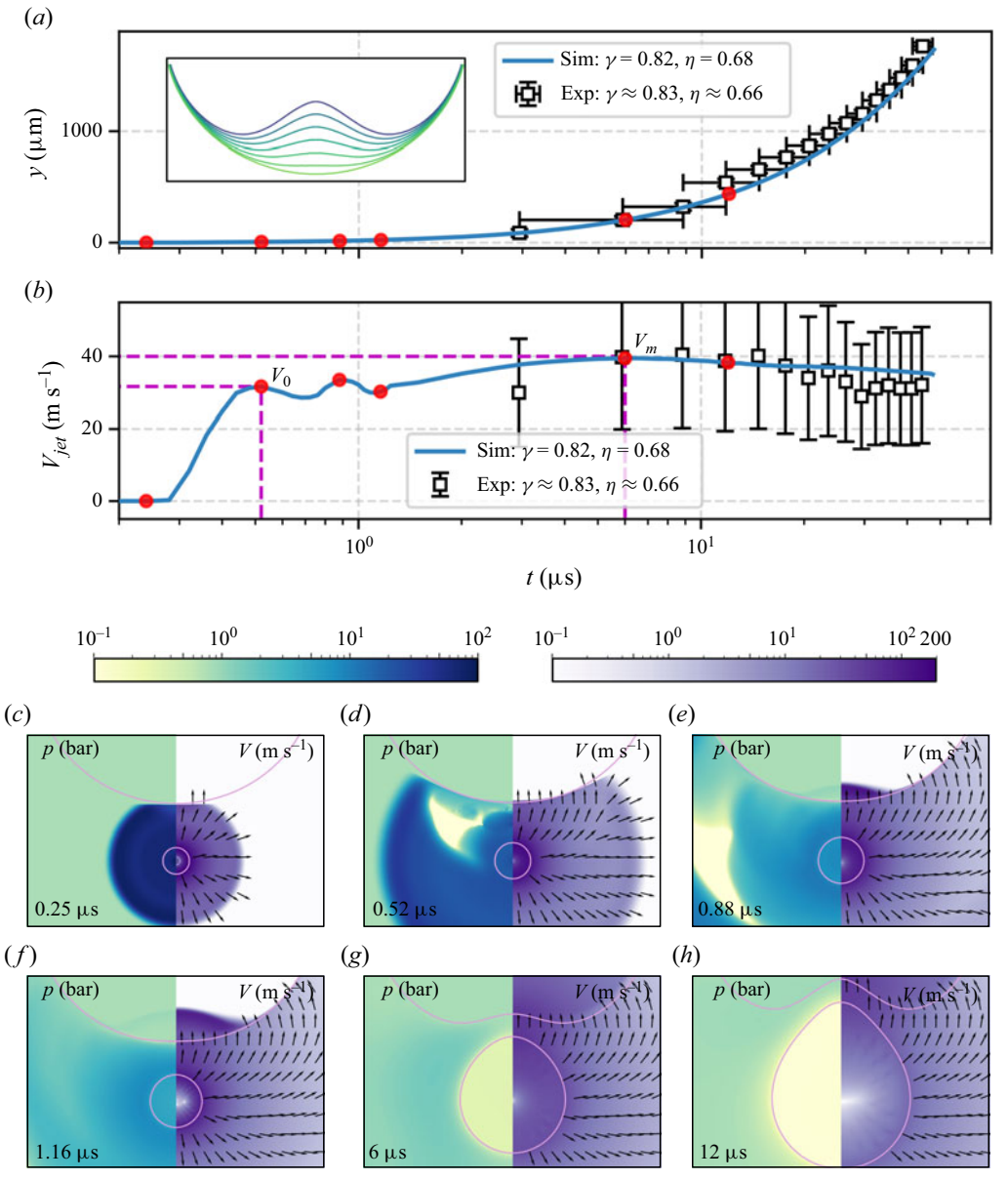


Figure 3. Evolution of a strong jet for a strong jet of $\gamma = 0.82$ and $\eta = 0.68$. (*a*) Vertical displacement of the air-bubble bottom surface and (*b*) jet velocity. The inset in panel (*a*) shows the jet tip deformation with time intervals of 2 μs. The pressure (left) and flow fields (right) are shown for the (*c–e*) initial acceleration stage and (*f–h*) jet focusing stage. Magnitudes are colour-coded and arrows indicate flow directions of the liquid phase. For a clear presentation, arrows in the region of approximately zero velocity are removed. Purple lines denote bubble interfaces. Each frame is 2 mm wide. Time instants for panels (*c*−*h*) are indicated by red dots in panels (*a*) and (*b*).

then undergoes a slight fluctuation and subsequently increases again to a peak value of approximately 40 m s^{-1}.

To give a detailed explanation of the above-mentioned tip development, the pressure and velocity fields at six representative time instants are shown in panels (*c*)−(*h*). These

https://doi.org/10.1017/jfm.2026.11575 Published online by Cambridge University Press

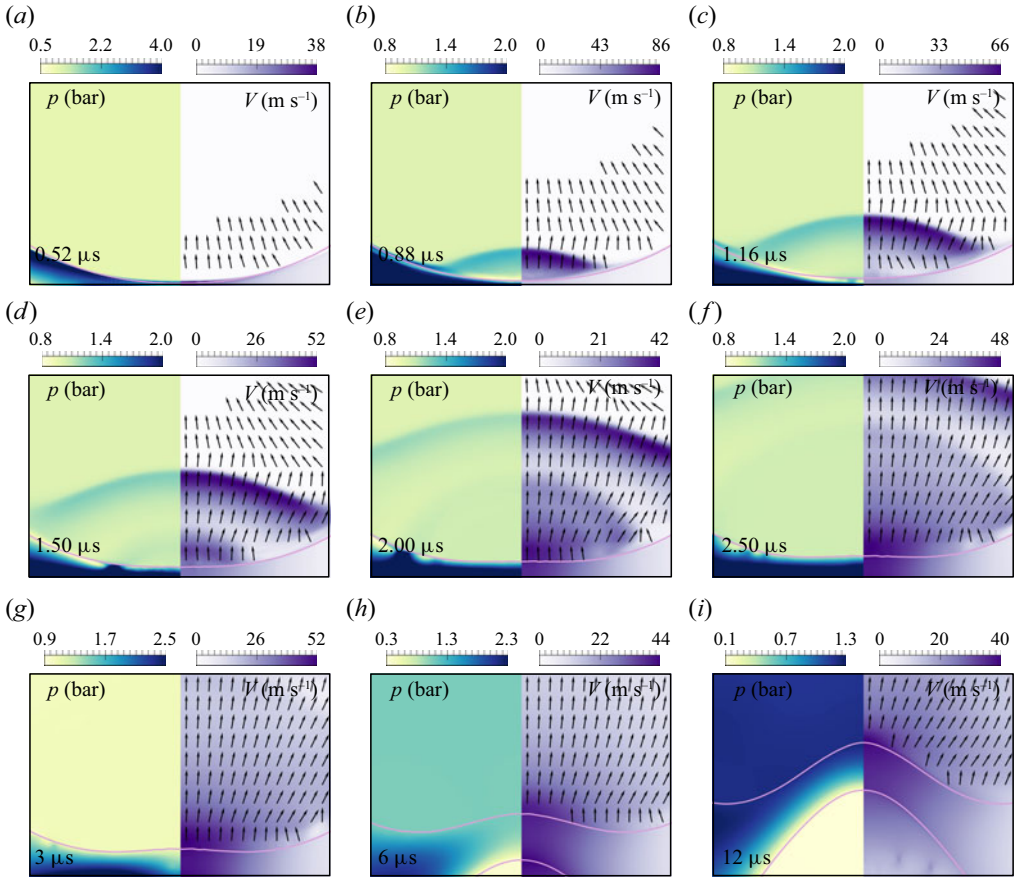


Figure 4. Pressure (left) and velocity (right) around the lower air–bubble interface during the flow focusing process of $\gamma = 0.82$ and $\eta = 0.68$. Arrows only indicate the directions of the air flow. Each frame is 1 mm wide.

instants are also marked as red dots on the curves of y and V_{jet}. Figure 3(*c*) shows that the nucleation shock wave reaches the air–liquid interface at $t \approx 0.25\ \mu$s with a peak pressure of 254 bar, driving the interface to a velocity of $32\ \mathrm{m\,s^{-1}}$ by $t \approx 0.5\ \mu$s. The subsequent fluctuation persists for less than 1 μs, after which the interface undergoes another acceleration, reaching $40\ \mathrm{m\,s^{-1}}$ at $t \approx 8\ \mu$s. This second acceleration arises from flow focusing: inspection of the velocity field shows that, immediately after the shock passage (e.g. at $t = 0.88\ \mu$s), the air inside the bubble attains velocities up to $90\ \mathrm{m\,s^{-1}}$, significantly exceeding the interface velocity; as the air flows upward, it entrains the interface, sustaining the focusing process for nearly 7 μs. Unlike the initial shock-induced acceleration, which is governed by the pressure impulse, flow focusing is a purely hydrodynamic process resulting from geometric confinement and inertial convergence of the liquid flow (Peters *et al.* 2013). Beyond $t \approx 9\ \mu$s, the jet decelerates despite the cavitation bubble moving closer.

The flow-focusing process is further shown in greater detail in figure 4, which reveals a complex evolution resulting from the coupled shock–interface interaction. At $t = 0.52\ \mu$s, the incident shock has accelerated the interface to $V_0 = 32\ \mathrm{m\,s^{-1}}$, while part of the shock is transmitted into the air bubble, increasing the velocity of the nearby air to approximately $38\ \mathrm{m\,s^{-1}}$. As the transmitted shock propagates through the bubble, the air velocity at the

https://doi.org/10.1017/jfm.2026.11575 Published online by Cambridge University Press

shock front first increases to approximately $86\,\mathrm{m\,s^{-1}}$ and then decreases as the shock diverges.

Focusing on the air motion near the interface, the adjacent air velocity begins to decrease at $t = 0.88\,\mu\mathrm{s}$, owing to the deceleration of the interface by the rarefaction wave on the liquid side (also see figure 3*e*), until the reflected shock in the liquid reaches the interface again at $t = 1.16\,\mu\mathrm{s}$. After $t = 1.5\,\mu\mathrm{s}$, the shock wave has decayed substantially and the rarefaction effect vanishes. Consequently, the air next to the interface remains faster than the interface, entraining the interface upward, until $t = 6\,\mu\mathrm{s}$. After that time, the air becomes slower than the interface because the flow direction becomes increasingly divergent, i.e. the focusing effect vanishes.

A third regime emerges at $\gamma \approx 0.66$ (figure 1*c*), where the cavitation bubble punctures the air bubble during its early expansion, creating an open cavity inside the air bubble. This process produces fine droplets that impinge on the upper interface, roughening it with spikes visible at $t = 9\,\mu\mathrm{s}$. The cavity subsequently collapses, forming two opposing jets that rupture both the air bubble apex and the lower cavitation bubble interface. We designate this regime as an explosive jet.

The explosive jet forms when the cavitation bubble is nucleated at very small separations, e.g. at $\gamma = 0.68$ and $\eta = 0.59$ (figure 5). The vertical movement y and velocity of the lower air–bubble interface V_{jet} are shown in figure 5(*a*,*b*). The inset of panel (*a*) presents the evolution of the lower air–bubble interface at intervals of $0.2\,\mu\mathrm{s}$, clearly illustrating the rupture dynamics. Both y and V_{jet} increase rapidly with time until rupture occurs. Unfortunately, experimental data are not available for this case because the temporal resolution is insufficient to resolve the rupture process.

In this case, the shock wave reaches the air–liquid interface at $t \approx 0.04\,\mu\mathrm{s}$ with a peak pressure of $\sim$1000 bar, imparting an average acceleration of $1.35 \times 10^9\,\mathrm{m\,s^{-2}}$. The shock wave accelerates the interface for $t \approx 0.2\mu\mathrm{s}$ to a velocity of approximately $270\,\mathrm{m\,s^{-1}}$. The interface then undergoes a second acceleration due to the flow focusing effect on a convex surface. As the liquid between the two bubbles becomes thinner, the interface ruptures at $t \approx 0.6\,\mu\mathrm{s}$ after attaining a velocity of $400\,\mathrm{m\,s^{-1}}$, while the cavitation bubble elongates into an egg shape with the upper surface reaching $460\,\mathrm{m\,s^{-1}}$. Following rupture, the bubble opens into a cavity and the high-speed gas continues to jet into the air bubble.

In this section, three distinct jet types are identified. All three undergo two stages of acceleration: an initial shock-induced acceleration followed by flow focusing on the concave air–liquid interface. The resulting jet velocity and subsequent dynamics, however, depend strongly on the separation between the laser-induced cavitation bubble and the air bubble. The jets are quantitatively classified as follows: weak jets, for which the jet travel distance satisfies $S < 2R_a$; strong jets, for which $S > 2R_a$; and explosive jets, for which rupture of the liquid film between the air bubble and the cavitation bubble occurs.

4. Jet tip velocity

Next, we first determine the initial jet velocity V_0 resulting from shock-induced acceleration from a simplified NS equation, then derive the jet velocity increment due to flow focusing based on flux conservation. In the following §§ 4 and 5, the experimental data are obtained from 90 experiments conducted under the same laser energy, and the simulations are conducted for a constant initial condition for the cavitation bubble with $R_0 = 40\,\mu\mathrm{m}$ and $p_0 = 2500$ bar. Therefore, the maximum radii of the cavitation bubble R_l for explosive jets can be determined as the mean experimental and computed radii, which are $568\,\mu\mathrm{m}$ and $546\,\mu\mathrm{m}$ with standard deviations of $31\,\mu\mathrm{m}$ and $17\mu\mathrm{m}$, respectively.

https://doi.org/10.1017/jfm.2026.11575 Published online by Cambridge University Press

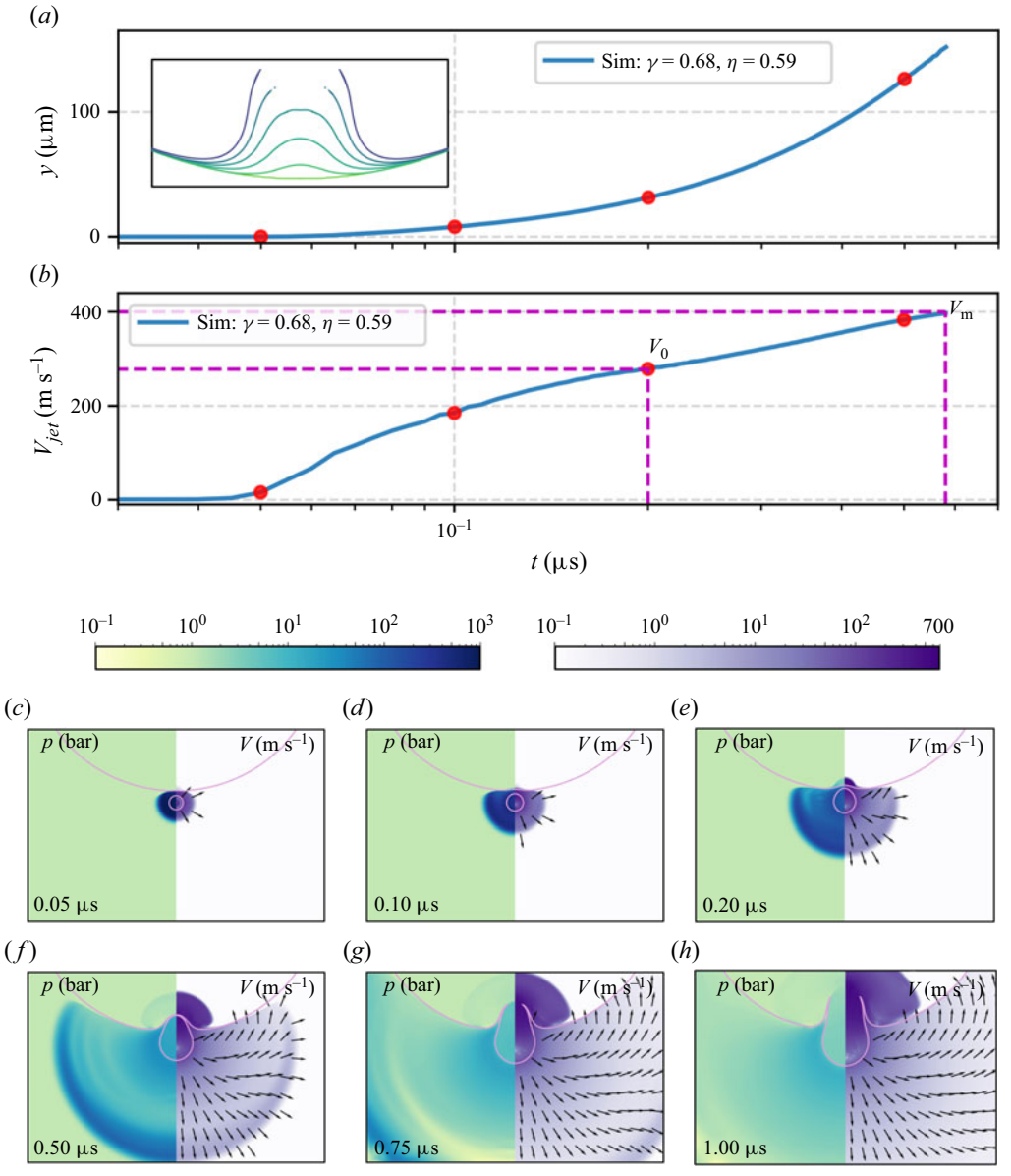


Figure 5. Evolution of an explosive jet for an explosive jet of $\gamma = 0.68$ and $\eta = 0.59$. (*a*) Vertical displacement of the air-bubble bottom surface and (*b*) jet velocity. The inset in panel (*a*) shows the jet tip deformation with time intervals of 0.2 μs. The pressure (left) and flow fields (right) are shown in panels (*c*−*h*). Magnitudes are colour-coded and arrows indicate flow directions of the liquid phase. For a clear presentation, arrows in the region of approximately zero velocity are removed. Purple lines denote bubble interfaces. Each frame is 2 mm wide. The time instants for panels (*c*−*h*) are marked as red dots in panels (*a*) and (*b*).

We first examine the pressure field. Figure 6 presents the spatio-temporal evolution of pressure for the weak-jet case shown in figure 2, with $\gamma = 1.14$ and $\eta = 0.70$. The air–liquid interface remains nearly stationary until the arrival of the initial shock wave at $t \approx 0.6$ μs. The propagation of this shock wave is clearly identified by tracking the location of the maximum pressure during $t = 0.3$–0.6 μs.

https://doi.org/10.1017/jfm.2026.11575 Published online by Cambridge University Press

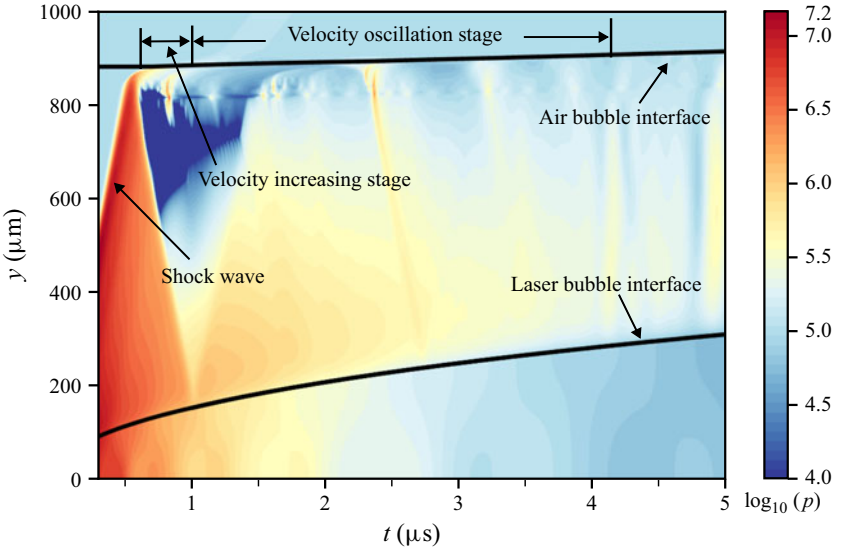


Figure 6. Spatio-temporal distribution of the pressure for $\gamma = 1.14$ and $\eta = 0.70$ during the early stage $t = 0.3{-}5\,\mu$s. A pressure range from 0.1 bar to 150 bar is chosen to highlight the pressure change. Here, the centre of the initial cavitation bubble is chosen as the origin of the y axis.

Following impact at $t \approx 0.6\,\mu$s, a localised high-pressure region persists near the air–liquid interface for approximately $0.4\,\mu$s, driving an initial acceleration of $2.75 \times 10^7\ \mathrm{m\,s^{-2}}$ and increase in interface velocity. The incident shock wave subsequently splits into a transmitted wave propagating inside the air bubble and a reflected wave travelling back into the liquid. This wave interaction produces a slightly elevated pressure within the air bubble and a reduced pressure in the liquid beneath it, reversing the pressure gradient across the interface and causing deceleration at $t \approx 1\,\mu$s.

The reflected wave is further reflected at the cavitation-bubble interface and propagates upward towards the air bubble, inducing a secondary acceleration upon re-impact. Owing to significant attenuation, this acceleration is weak. Repeated wave reflections between the two interfaces lead to oscillatory motion of the jet tip, consistent with the velocity fluctuations observed in figure 2(*b*).

Focusing on the motion of the lower air–liquid interface, its acceleration can be obtained by simplifying the Navier–Stokes equation under the pressure loading imposed by the flow:

$$\frac{\mathrm{D}V}{\mathrm{D}t} = \frac{1}{\rho}\frac{p - p_b}{\delta}, \tag{4.1}$$

where $\mathrm{D}V/\mathrm{D}t$ is the material derivative of the flow velocity of the tip, p denotes the local high pressure near the interface, p_b is the pressure of the air bubble, and δ is the distance between the interface and the high pressure p location. Since the shock wave acts as a short pressure pulse, the induced jet velocity can be estimated using the peak pressure p_m and the duration of the pulse Δt while considering $p_m \gg p_b$:

$$V_0 \approx \frac{p_m \Delta t}{2\rho\delta}. \tag{4.2}$$

For a spherical blast wave generated by laser-induced cavitation, Vogel, Busch & Parlitz (1996) showed experimentally that the peak pressure scales as

https://doi.org/10.1017/jfm.2026.11575 Published online by Cambridge University Press

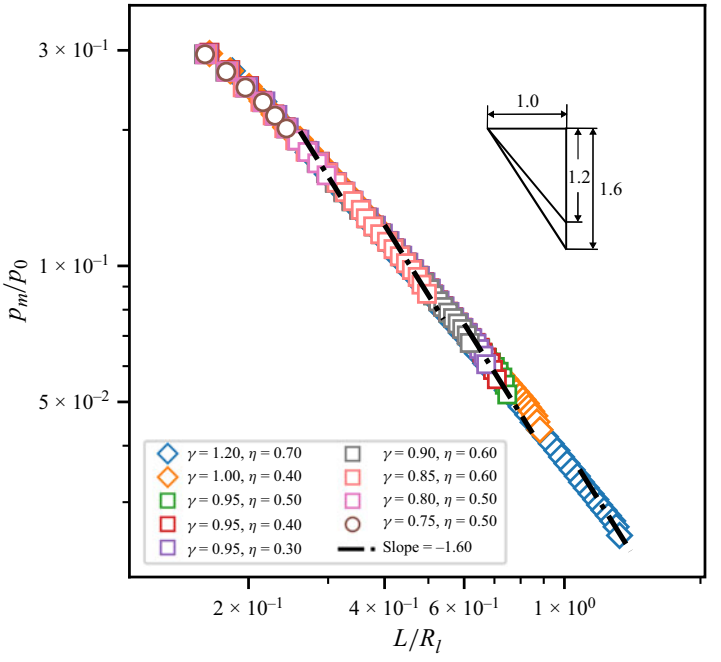


Figure 7. Pressure decay along its propagation for nine representative conditions covering all three jetting regimes. All data decrease with a similar slope of −1.2 initially, but slightly increases along the propagation path. A steeper decay $n \approx -1.6$ is observed very close to the air bubble interface for all the cases.

$$p_m \propto p_0 \left(\frac{L}{R_l}\right)^n, \tag{4.3}$$

where p_0 is the initial bubble pressure and L is the distance from bubble centre to the location of p_m. Additionally, n is the decade exponent during the wave propagation, a complex function of wave source, travel distance and pressure values.

For comparable conditions, Vogel *et al.* (1996) experimentally reported decay exponents ranging from −1.0 to −2.0. More recently, Bokman *et al.* (2023) used the open-source solver ECOGEN to simulate shock-wave propagation with pressure profiles prescribed from laser-induced shock-wave measurements, obtaining an exponent of −1.4. Notably, neither study considered shock-wave decay in the presence of a nearby interface.

To determine the decay exponent, the normalised peak pressure p_m/p_0 is plotted against the normalised distance L/R_l for nine cases spanning different γ and η in figure 7. Data across all three jetting regimes exhibit a similar trend with a varying slope: an initial decay with exponent $n = -1.2$, then slight increases as the pressure approaches the air-bubble interface (the end of each marker-line). The slope changes to $n \approx -1.6$ in the vicinity of the air bubble. This region corresponds to the location where the elevated pressure produces significant interface acceleration. Accordingly, $n = -1.6$ is adopted to estimate the shock-induced acceleration of the interface.

Since δ is proportional to R_l, $\Delta t \sim 2R_0/c$ with c the speed of sound in water and $L = d - R_a$, the jet velocity V_0 could be written as

$$V_0 = \beta \frac{p_0}{\rho c} \frac{R_0}{R_l} \left(\frac{\gamma(1+\eta) - 1}{\eta}\right)^n, \tag{4.4}$$

https://doi.org/10.1017/jfm.2026.11575 Published online by Cambridge University Press

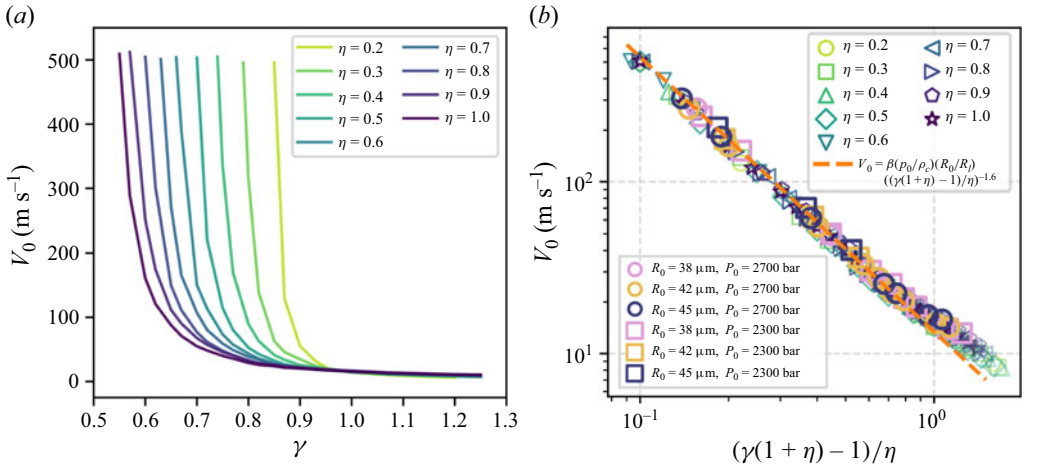


Figure 8. (*a*) Jet velocities due to the acceleration by initial shock wave as a function of γ from simulation. (*b*) All simulated data collapse onto an orange dashed line $V_0 = (\beta p_0 R_0/\rho c R_l)((\gamma(1+\eta)-1)/\eta)^{-1.6}$. The opacity of the marks from dark to light represents increasing γ. The purple dashed line $(\gamma(1+\eta)-1)/\eta = 0.25$ is the transition from explosive to strong jet regime.

with $\beta = \mathcal{O}(1)$ the only proportionality factor. Figure 8(*a*) shows V_0 as a function of γ for nine values of η, where V_0 decreases rapidly with increasing γ. In figure 8(*b*), all data collapse onto (4.4) using $\beta = 1.1$, and the numerical initial conditions $p_0 = 2500$ bar and $R_0 = 40\,\mu$m. Six additional data sets covering two different values of p_0 and three different initial bubble radii R_0 are also included in the plot. The average decay exponent is chosen as $n = -1.6$.

During the second phase of jet formation, the flow focusing effect is only significant in the strong jet regime: in the weak-jet regime, the air velocity is too small, while in the explosive regime, rupture occurs too early for flow focusing to develop. For a short time Δt_f after V_0, the velocity increase $\mathrm{d}V$ due to a small reduction of the air-bubble radius R_a satisfies a flux-conservation relation:

$$V_0 R_a^2 = (V_0 + \mathrm{d}V)\,(R_a - \mathrm{d}R)^2\,. \tag{4.5}$$

Neglecting higher-order terms, with $\mathrm{d}R = V_0\,\mathrm{d}t$, the acceleration due to flow focusing reduces to $a = \mathrm{d}V/\mathrm{d}t = 2V_0^2/R_a$. The focusing time scale is $\Delta t_f \approx h/V_0$, where h is the travel distance to the location of peak velocity. Here, h is defined as the axial distance from the initial air–liquid interface beyond which the interface velocity begins to decelerate (see figure 9*a* inset). From the perspective of flow focusing, h corresponds to the location of minimum cross-sectional area along the jet. In the present configuration, h depends on both the curvature of the air–liquid interface and the divergence of the flow induced by the expanding spherical cavitation bubble. Accordingly, it may be expressed in dimensionless form as $h/R_a = \eta^b f(\gamma)$, where the factor η^b accounts for the effect of interface curvature and $f(\gamma)$ represents the influence of flow divergence. The exponent $b = \mathcal{O}(1)$ ensures that h depends only on γ in the limit of a flat interface ($R_a \to \infty$). Figure 9(*a*) shows good agreement between this scaling and the numerical results, yielding the empirical relation $(h/R_a)\eta^{-0.75} = 0.4 - 0.25\gamma$.

Substitution gives $V_m = V_0 + a\Delta t = (1 + (0.8 - 0.5\gamma)\eta^{0.75})V_0$. In figure 9, we plot the normalised jet velocity $V_m^* = V_m/(1 + (0.8 - 0.5\gamma)\eta^{0.75})/(\beta p_0 R_0/\rho c R_l)$ of the experimental and simulation data. In the experiments, the jet velocity as a function of time is obtained by temporal differentiation of the jet-tip position. Due to the limited temporal

https://doi.org/10.1017/jfm.2026.11575 Published online by Cambridge University Press

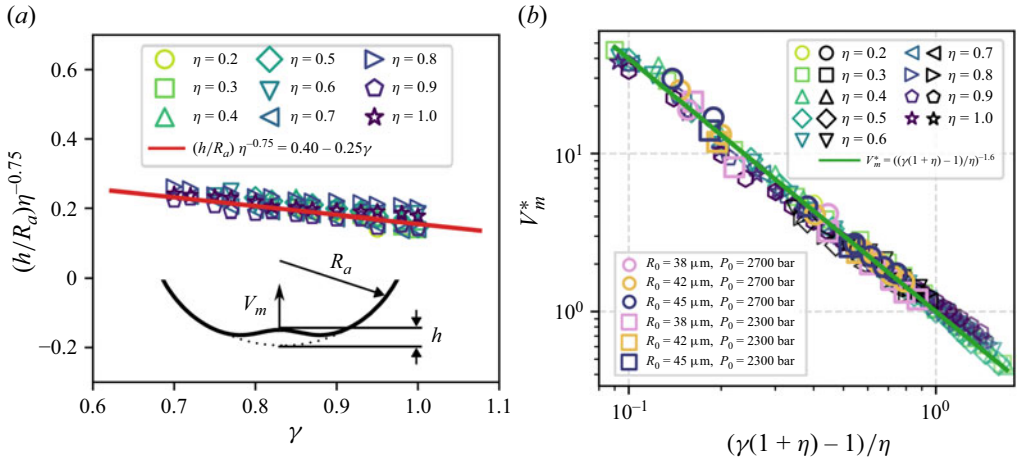


Figure 9. (*a*) $(h/R_a)\eta^{-0.75}$ as a function of γ for eight sets of simulation data in the strong jet regime. The red line denotes a linear relation $(h/R_a)\eta^{-0.75} = 0.40 - 0.25\gamma$. (*b*) Experimental (dark open symbols) and simulation data for the normalised maximum velocity $V_m^* = V_m/(1 + (0.8 - 0.5\gamma)\eta^{0.75})/(1.1\,p_0 R_0/\rho c R_l)$.

resolution of 2.94 µs, the experiments cannot resolve the shock-wave acceleration stage for weak and strong jets, nor the rupture velocity in the explosive-jet regime. Therefore, V_m is defined as the maximum measured tip velocity for the experimental data. We find all data collapse onto the theoretical curve $V_m^* = ((\gamma(1+\eta) - 1)/\eta)^{-1.6}$ in all three jetting regimes. The results suggest that in the current configuration, the flow focusing effect is a complex function of η and γ. The velocity increment is $(0.8 - 0.5\gamma)\eta^{0.75}V_0$, with η reflecting the influence of the liquid–air interface curvature and γ affecting the divergence of the flow induced by the spherical shock-wave. This robust mechanism offers a route to tuneable jet formation with

$$V_m = 1.1\left(1 + (0.8 - 0.5\gamma)\eta^{0.75}\right)\frac{p_0}{\rho c}\frac{R_0}{R_l}\left(\frac{\gamma(1+\eta) - 1}{\eta}\right)^{-1.6}. \tag{4.6}$$

Similarly, the interaction between a planar shock wave and an air bubble is found to be mainly an acceleration-driven process (Bokman *et al.* 2025). There the jet velocity can be predicted through an acceleration-induced interfacial-stability analysis, where the pressure impulse determines the magnitude of the acceleration and the acceleration duration influences the impulsive growth of interfacial perturbations.

5. Jetting regime

Figure 10(*a*) summarises the distribution of the three types of jets on the (η, γ) parametric map. The dark dashed line $\gamma = 1/(\eta + 1)$ marks the condition for initial coalescence of the air and cavitation bubbles. From experiments and simulation, we find that explosive jets occur when $(d - R_a)/R_l < 0.25$, yielding the transition $\gamma = 1/4 + 3/(4(\eta + 1))$. In the limit $\eta \to \infty$, this condition reduces to $\gamma = 0.25$, corresponding to the rupture condition of a free surface by an underlying cavitation bubble, as reported in previous experimental studies (Rosselló *et al.* 2022; Wang *et al.* 2025). The transition boundary between explosive and strong jets decreases with increasing η, consistent with experimental observations. To estimate the threshold for strong jet formation, we consider the condition when the jet reaches the upper surface and recoils, i.e. $S = 2R_a$. At this point, the balance for a capillary-arrested tip is $1/2\rho V_l^2 \approx 2\sigma/r_{jet}$, where V_l is the average velocity of the

https://doi.org/10.1017/jfm.2026.11575 Published online by Cambridge University Press

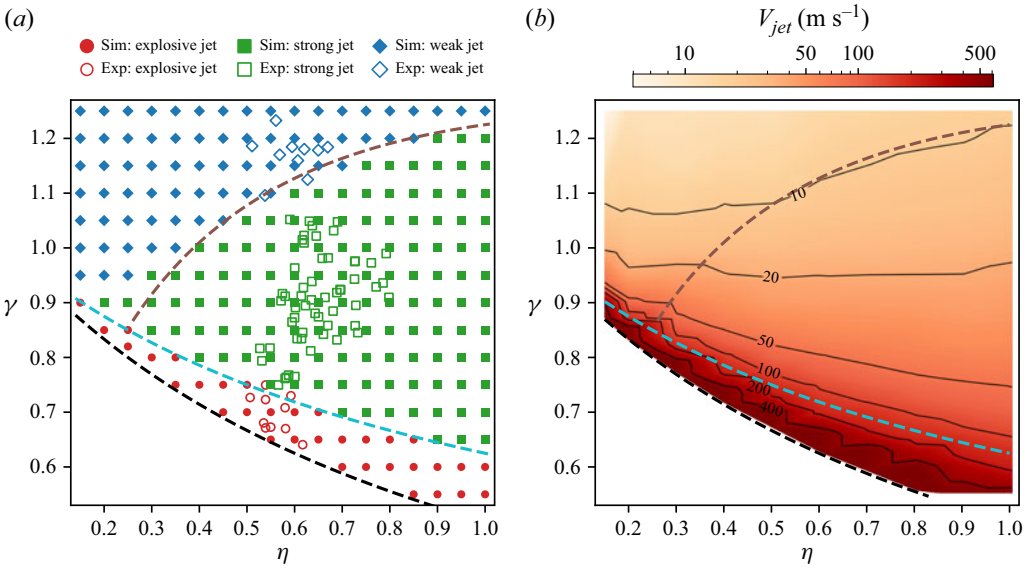


Figure 10. Distribution of (*a*) jet types and (*b*) jet velocities in a (η, γ) parametric map. Open and filled symbols are experimental and computed results, respectively. Circle, square and rhombus symbols represent explosive jet, strong jet and weak jet, respectively. In panel (*b*), the contours of jet velocity are plotted in a log-scale. The dark dashed line is the condition for initial coalescence of the air and cavitation bubbles $\gamma = 1/(\eta + 1)$. The cyan dashed line is $\gamma = 1/4 + 3/(4(\eta + 1))$. The brown dashed line is $\gamma = 2.45\eta^{0.6}/(1 + \eta)$.

whole jet and is proportional to the tip velocity V_m and $r_{jet} \propto R_a$ is the jet base radius. The scaling gives $V_m \approx \kappa\sqrt{4\sigma/\rho R_a}$ with κ a proportional factor. Combining this estimate with (4.6) yields the criterion for strong jet formation:

$$\left(1 + (0.8 - 0.5\gamma)\eta^{0.75}\right)\frac{p_0}{\rho c}\frac{R_0}{R_l}\left(\frac{\gamma(1+\eta) - 1}{\eta}\right)^{-1.6} > \kappa\sqrt{4\sigma/(\rho R_a)}. \tag{5.1}$$

At the boundary between strong and weak jets, $(0.8 - 0.5\gamma)\eta^{0.75} = \mathcal{O}(0.1)$; therefore, the previous equations can be further simplified in a dimensionless form:

$$\gamma < g\left(\frac{k\eta^{0.69} + 1}{1 + \eta}\right), \tag{5.2}$$

with two factors k and g accounting for the proportional influence. Yet from the data, we obtain a similar condition of $\gamma < 2.45\eta^{0.6}/(1 + \eta)$. This expression provides a quantitative threshold separating weak and strong jet regimes, linking jet formation directly to bubble-size ratio η and relative distance γ. The model predicts strong-jet formation for $\eta > 0.25$, while the simulations indicate a slightly lower threshold of $\eta \geqslant 0.2$.

Figure 10(*b*) shows simulated jet velocities contours in log-scale in the same (η, γ) map. Jet speed is taken as the tip velocity after flow focusing for weak and strong jets, and just before rupture for explosive jets. Velocities increase towards the lower-left of the (η, γ) map, reaching $\sim$600 m s^{-1} near the coalescence condition. For strong jets, the maximum occurs along $\gamma = 1/4 + 3/(4(\eta + 1))$, where V_0 is the same. Equation (4.6) then gives

$$V_m = \left(1 + \left(0.8 - 0.5 \times \left(\frac{1}{4} + \frac{3}{4(\eta + 1)}\right)\right)\eta^{0.75}\right)V_0, \tag{5.3}$$

https://doi.org/10.1017/jfm.2026.11575 Published online by Cambridge University Press

demonstrating that jet velocity increases with η, i.e. the normalised curvature of the air bubble.

The previous analysis focuses on the roles of the geometric parameters γ and η. However, fluid properties such as viscosity and surface tension may also exert an important influence on the jet dynamics, as indicated by previous studies of jet formation following air-bubble rupture and pressure impulse (Lai *et al.* 2018; Gordillo, Onuki & Tagawa 2020; Gordillo & Blanco-Rodríguez 2023). In particular, viscous effects tend to reduce the flow velocity and promote the formation of a thinner jet, whereas surface tension stabilises the interface and resists jet breakup. Inclusion of these effects would extend the governing parameter space to (γ, η, We, Oh), where We and Oh are the Weber and Ohnesorge numbers, respectively. A systematic investigation in this enlarged parameter space lies beyond the scope of the present work, but would be an interesting direction for future study.

6. Conclusion

In summary, we investigated the jetting of an air bubble driven by the expansion and collapse of a nearby cavitation bubble. Using high-speed imaging and compressible VoF simulations, we identified three distinct jet types – weak, strong and explosive – governed by the stand-off distance γ and size ratio η. Jet formation proceeds through two stages of acceleration: initial shock-induced motion and subsequent flow focusing. Formulae were derived for both mechanisms, showing close agreement with experimental and numerical results. The initial shockwave accelerates the air bubble interface to a velocity of $V_0 = 1.1 p_0 R_0/(\rho c R_l)((\gamma(1+\eta)-1)/\eta)^{-1.6}$, while the flow focusing effect is only significant in the strong jet regime, amplifying the interface to $V_m = (1 + (0.8 - 0.5\gamma)\eta^{0.75})V_0$. We further summarise phase diagrams for the distribution and velocity of three types of jets on a parametric map of (η, γ). Transitions between regimes were derived theoretically, accurately predicting observed jet morphologies. These results demonstrate that jet formation depends non-trivially on η and γ, offering a robust pathway for controlled jet modulation.

Acknowledgements. We thank Beng Hau Tan for insightful discussion. The anonymous referees are acknowledged for their very helpful suggestions to improve the manuscript.

Funding. This research was partly funded by the National Natural Science Foundation of China under grant nos. 12302313 and 52525102, the Fundamental Research Funds for the Central Universities under grant no GK762026011542, and supported by National Key Laboratory of Marine Engine Science and Technology.

Declaration of interests. The authors report no conflict of interest.

Author contributions. S.L. and B.W. have contributed equally to the manuscript.

Appendix A. Sensitivity analysis of the jet formation

A mesh-sensitivity analysis was performed for the jet formation process using five grid spacings, $\Delta x = 7.81$, 3.21, 2.60, 2.23 and 1.95 µm. Figure 11 compares the time evolution of the vertical position of the air-bubble bottom interface in panel (a) and its velocity in panel (b) for the strong jet case shown in figure 1(b). With decreasing grid spacing, both the interface position and jet velocity exhibit clear convergence. In particular, the results obtained with $\Delta x = 2.23$ and 1.95 µm are nearly indistinguishable. Balancing numerical accuracy and computational efficiency, a grid spacing of $\Delta x = 2.23$ µm is chosen throughout this study.

https://doi.org/10.1017/jfm.2026.11575 Published online by Cambridge University Press

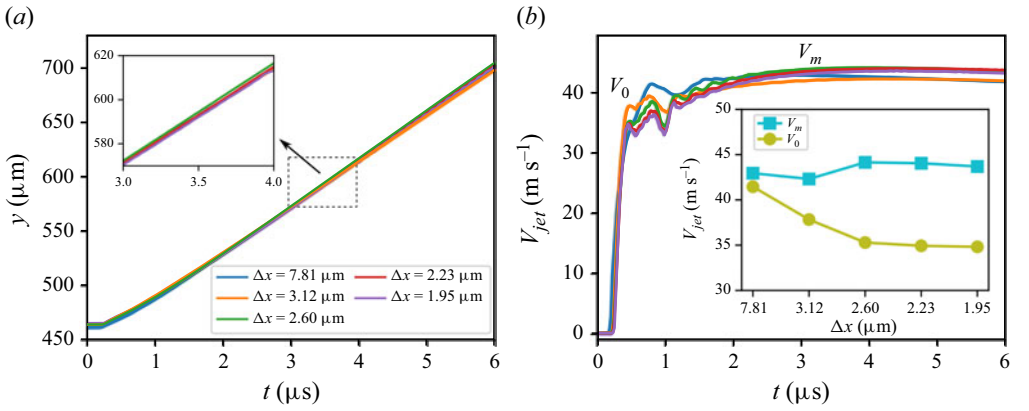


Figure 11. Dynamics of bubble bottom surface under different mesh resolutions: (*a*) position versus time; (*b*) jet velocity versus time. Inset of panel (*b*) shows the jet velocity versus grid spacing.

References

Bokman, G.T., Biasiori-Poulanges, L., Lukić, B., Brill, S.R., Bourquard, C., Olson, B.J., Rack, A. & Supponen, O. 2025 Shock-induced bubble jets: a dual perspective of bubble collapse and interfacial instability theory. *J. Fluid Mech.* **1018**, A9.

Bokman, G.T., Biasiori-Poulanges, L., Meyer, D.W. & Supponen, O. 2023 Scaling laws for bubble collapse driven by an impulsive shock wave. *J. Fluid Mech.* **967**, A33.

Eggers, J. 1997 Nonlinear dynamics and breakup of free-surface flows. *Rev. Mod. Phys.* **69** (3), 865.

Eggers, J. & Villermaux, E. 2008 Physics of liquid jets. *Rep. Prog. Phys.* **71** (3), 036601.

Fan, Y., Bussmann, A., Reuter, F., Bao, H., Adami, S., Gordillo, J.M., Adams, N. & Ohl, C.-D. 2024 Amplification of supersonic microjets by resonant inertial cavitation-bubble pair. *Phys. Rev. Lett.* **132** (10), 104004.

Gekle, S., Peters, I.R., Gordillo, J.M., van der Meer, D. & Lohse, D. 2010 Supersonic air flow due to solid–liquid impact. *Phys. Rev. Lett.* **104** (2), 024501.

Gordillo, J.M. & Blanco-Rodríguez, F.J. 2023 Theory of the jets ejected after the inertial collapse of cavities with applications to bubble bursting jets. *Phys. Rev. Fluids* **8** (7), 073606.

Gordillo, J.M., Onuki, H. & Tagawa, Y. 2020 Impulsive generation of jets by flow focusing. *J. Fluid Mech.* **894**, A3.

Han, B., Köhler, K., Jungnickel, K., Mettin, R., Lauterborn, W. & Vogel, A. 2015 Dynamics of laser-induced bubble pairs. *J. Fluid Mech.* **771**, 706–742.

Kiyama, A., Tagawa, Y., Ando, K. & Kameda, M. 2016 Effects of a water hammer and cavitation on jet formation in a test tube. *J. Fluid Mech.* **787**, 224–236.

Koch, M., Lechner, C., Reuter, F., Köhler, K., Mettin, R. & Lauterborn, W. 2016 Numerical modeling of laser generated cavitation bubbles with the finite volume and volume of fluid method, using OpenFOAM. *Comput. Fluids* **126**, 71–90.

Lai, C.-Y., Eggers, J. & Deike, L. 2018 Bubble bursting: universal cavity and jet profiles. *Phys. Rev. Lett.* **121** (14), 144501.

Lohse, D. 2022 Fundamental fluid dynamics challenges in inkjet printing. *Annu. Rev. Fluid Mech.* **54** (1), 349–382.

Luo, J., Xu, W. & Khoo, B.C. 2021 Stratification effect of air bubble on the shock wave from the collapse of cavitation bubble. *J. Fluid Mech.* **919**, A16.

Maeda, K. & Fuster, D. 2024 Regressing bubble cluster dynamics as a disordered many-body system. *J. Fluid Mech.* **985**, A23.

Miller, S.T., Jasak, H., Boger, D.A., Paterson, E.G. & Nedungadi, A. 2013 A pressure-based, compressible, two-phase flow finite volume method for underwater explosions. *Comput. Fluids* **87**, 132–143.

Mishra, A., Bourquard, C., Roy, A., Lakkaraju, R., Ghosh, P. & Supponen, O. 2022 Flow focusing from interacting cavitation bubbles. *Phys. Rev. Fluids* **7** (11), 110502.

Mnich, D., Reuter, F., Denner, F. & Ohl, C.-D. 2024 Single cavitation bubble dynamics in a stagnation flow. *J. Fluid Mech.* **979**, A18.

https://doi.org/10.1017/jfm.2026.11575 Published online by Cambridge University Press

PETERS, I.R., TAGAWA, Y., OUDALOV, N., SUN, C., PROSPERETTI, A., LOHSE, D. & VAN DER MEER, D. 2013 Highly focused supersonic microjets: numerical simulations. *J. Fluid Mech.* **719**, 587–605.

ROSSELLÓ, J.M., REESE, H. & OHL, C.-D. 2022 Dynamics of pulsed laser-induced cavities on a liquid–gas interface: from a conical splash to a 'bullet'jet. *J. Fluid Mech.* **939**, A35.

TAGAWA, Y., OUDALOV, N., VISSER, C.W., PETERS, I.R., VAN DER MEER, D., SUN, C., PROSPERETTI, A. & LOHSE, D. 2012 Highly focused supersonic microjets. *Phys. Rev. X* **2** (3), 031002.

TOMITA, Y. & SATO, K. 2017 Pulsed jets driven by two interacting cavitation bubbles produced at different times. *J. Fluid Mech.* **819**, 465–493.

VISSER, C.W., TAGAWA, Y., SUN, C. & LOHSE, D. 2012 Microdroplet impact at very high velocity. *Soft Matt.* **8** (41), 10732–10737.

VOGEL, A., BUSCH, S. & PARLITZ, U. 1996 Shock wave emission and cavitation bubble generation by picosecond and nanosecond optical breakdown in water. *J. Acoust. Soc. Am.* **100** (1), 148–165.

WANG, G., WANG, J., CHEN, X., HUANG, J., SONG, G., ZENG, Q. & WANG, Y. 2025 Partial ventilation of an oscillating bubble induced by Rayleigh–Taylor instability near a water surface. *Phys. Rev. Fluids* **10** (12), 123601.

WELLER, H.G., TABOR, G., JASAK, H. & FUREBY, C. 1998 A tensorial approach to computational continuum mechanics using object-oriented techniques. *Comput. Phys.* **12** (6), 620–631.

ZEFF, B.W., KLEBER, B., FINEBERG, J. & LATHROP, D.P. 2000 Singularity dynamics in curvature collapse and jet eruption on a fluid surface. *Nature* **403** (6768), 401–404.

ZENG, Q., AN, H. & OHL, C.-D. 2022 Wall shear stress from jetting cavitation bubbles: influence of the stand-off distance and liquid viscosity. *J. Fluid Mech.* **932**, A14.

ZENG, Q., GONZALEZ-AVILA, S.R., VOORDE, S.T. & OHL, C.-D. 2018 Jetting of viscous droplets from cavitation-induced Rayleigh–Taylor instability. *J. Fluid Mech.* **846**, 916–943.

ZENG, Q., ZHANG, A.-M., TAN, B.H., AN, H. & OHL, C.-D. 2024 Jetting enhancement from wall-proximal cavitation bubbles by a distant wall. *J. Fluid Mech.* **987**, R2.

ZHANG, A.-M., LI, S.-M., XU, R.-Z., PEI, S.-C., LI, S. & LIU, Y.-L. 2024 A theoretical model for compressible bubble dynamics considering phase transition and migration. *J. Fluid Mech.* **999**, A58.

https://doi.org/10.1017/jfm.2026.11575 Published online by Cambridge University Press